Available online at https://ganitjournal.bdmathsociety.org/

GANIT: Journal of Bangladesh Mathematical Society

GANIT *J. Bangladesh Math. Soc.* 44.2 (2024) 077–096
DOI: https://doi.org/10.3329/ganit.v44i2.78536

Convective Heat Transfer in the Strongly Viscous Mantle in Different Aspect Ratio Cells

Tania S. Khaleque *[a], Noushin A. Trina[a], and Sumaiya B. Islam [b]

[a] *Department of Applied Mathematics, University of Dhaka, Dhaka - 1000, Bangladesh*
[b] *Department of Mathematics, Bangabandhu Sheikh Mujibur Rahman Maritime University, Dhaka - 1216, Bangladesh*

ABSTRACT

Mantle convection, a fundamental mechanism controlling the dynamics of the Earth's surface and interior, shows different behaviors caused by different factors such as viscosity variation, viscous dissipation, internal heating, and so on. In this paper, the effects of temperature-dependent viscosity, temperature and pressure-dependent viscosity and viscous dissipation on mantle convection are investigated in elongated and narrow cells. The Rayleigh-Bénard convection model is solved numerically with the full form of the Arrhenius viscosity function at a high Rayleigh number for viscosity contrasts up to 10^{30}. The root mean square velocity and Nusselt number are computed and tabulated. The thermal characteristics and flow dynamics inside the convection cell are presented by temperature profiles and stream function contours. These simulated results indicate that increasing viscosity contrasts with the incorporation of viscous dissipation weakens the convection vigour and heat transfer in the mantle. The selected narrow cell remains stable for a very high viscosity contrast at different viscous pressure number μ, whereas the selected elongated cell with temperature-dependent viscosity and strong viscous dissipation becomes unstable and single-cell pattern breaks down at high viscosity variation.

Received: November 17, 2024 **Accepted:** December 15, 2024 **Published Online:** December 30, 2024

Keywords: Mantle convection; Variable viscosity; Viscous dissipation; Elongated cell; Narrow cell
AMS Subject Classifications 2024: 76D05, 80A19, 8610.

1 Introduction

For a long time, scientists have been ridiculed by the geological processes that led to the formation of ice ages, earthquakes, volcanoes, mountain ranges, sea floor spreading, and sedimentary basins. The long-awaited explanation to these queries has been provided by the concept of mantle convection and plate tectonics theory [1, 2]. Arthur Holmes [3, 4] was the first to propose the idea of the convection in the mantle. Mantle convection modifies the planetary surfaces and propels geological activity and for a long period of time, it has been the driving mechanism of various physical phenomena [5].

The composition of mantle is very intricate and a number of factors influences the mantle. Viscosity is one of the most distinctive and significant features of the mantle. According to standard parameter values relevant to the Earth, there is a viscosity difference of order 10^{50} across the mantle depth of about 3000 km [6]. A recent

*Corresponding author. *E-mail address:* tania.khaleque@du.ac.bd

study reveals that the viscosity of the upper mantle is around 2.8×10^{22} Pa s [7]. Mantle viscosity is strongly influenced by temperature, pressure and stress [2]. Turcotte and Oxburgh [8] did the first boundary layer analysis for mantle convection with constant viscosity in 1967. Later mantle convection with variable viscosity was investigated by many studies [9, 10, 11, 12, 13]. According to the investigation of Jain and Solomatov [14] on convection with highly temperature-dependent viscosity, a high-viscosity stationary lid develops at the upper surface as the viscosity gradient expands, leading to Rayleigh-Bénard-like convection in a sublayer underneath it. Jain and Solomatov [15] used 2D numerical simulations to investigate convection with temperature-dependent viscosity below the critical Rayleigh number. The concurrent effects of temperature- and pressure-dependent rheology on convection and geoid above the plumes were studied by Shahraki and Schmeling [16] in a 2D axi-symmetrical model. A few more significant 2D Cartesian geometry computational models that analyze mantle convection are carried out by Gassmöller et al. [17], Agrusta et al. [18], Khaleque and Motaleb [19], Agarwal et al. [20], Khaleque et al. [21], Capitanio et al. [22], Whitehead [23], Kameyama [24], Okuda and Takehiro [25], Trim et al. [26]. For the first time, Blankenbach et al.[27] benchmarked the values of some significant physical quantities of mantle convection. Recently, Trim et al. [28] studied a series of thermochemical mantle convection problems in 2D and produced some benchmark values.

Viscous dissipation is another influential characteristic of mantle convection. According to Leng and Zhong [29], for temperature-dependent viscosity, only less than 10% of the total dissipation is accounted for by bending dissipation alone. Approximately 86% of the gravitational energy is converted into heat by viscous dissipation when the slab subducts [30]. Goni et al. [31] showed that viscous dissipation reduces the intensity of convection, but the addition of internal heating and an increased viscous pressure number strengthen it. A recent study conducted by Islam et al. [32] shows that with increasing viscosity contrast and viscous dissipation number, convection becomes weaker. In simulations of rotating, density-stratified flat strata of convection, Lance et al. [33] offer the first comprehensive analysis of viscous dissipation. Regarding viscous dissipation in mantle convection, some recent investigations done by Requilé et al. [34], Straughan [35], Knight et al. [36] are particularly noteworthy.

For boundaries without stress, oscillatory convection begins at comparatively low Rayleigh numbers. Above a particular Rayleigh number, single cells with aspect ratio of a = 2.5 remain stable at least upto a higher Rayleigh number, but cells with an aspect ratio a = 4.0 split up into multiple short cells. Convection in the Earth's mantle is most likely to take the shape of long-wavelength cells [37]. In an enclosure with uniform and sinusoidal temperatures, the effects of ratio of aspect and nonuniform temperature on mixed convection are investigated. It displays notable variations in the sinusoidal localized thermal exchange rate and flow rate [38].

Because of its complexity, full understanding of the movement of the Earth's mantle and representing this numerically in a fitting way is one of the most difficult challenges of the present day. Though several studies have been carried out in the area of mantle convection to investigate its cell pattern under the effect of different parameters and different cell size, for the particular rectangular cell size 1:2 (narrow) and 2:1 (elongated) with high temperature-dependent viscosity variation as well as temperature-and pressure-dependent viscosity variation with viscous dissipation effect have not been investigated before. In this paper, the aim is to search for convection cell patterns by examining high Rayleigh number convection in the mantle in narrow and elongated cells with variable viscosity and viscous dissipation. Very high viscosity contrast across the mantle layer is considered here so that it closely represents the mantle viscosity. The governing equations together with the relevant boundary conditions for mantle convection and the full form Arrhenius viscosity function are described in section 2. Then non-dimensionalization of the equations are carried out and dimensionless parameters are obtained. In section 3, the computation and simulation approach are explained and the process is validated by comparing our computed results with benchmark values and earlier studies. Then in section 4 we solve our specific Rayleigh-Bénard convection model in two cells of aspect ratios 1:2 (narrow) and 2:1 (elongated) and present the simulated results using graphs and tables. Finally, a few conclusions drawn from the findings are discussed in section 5. To the best of our knowledge, such high viscosity variation (up to 10^{30}) due to temperature-dependent viscosity and temperature- and pressure-dependent viscosity with viscous dissipation in narrow and elongated convection cells has not been studied before.

2 Governing Equations

A classical two-dimensional Rayleigh-Bénard convection model is taken into consideration for this study. A rectangular domain with boundaries extending horizontally across the cell are considered to have a constant temperature contrast between them (Figure 2.1). In the corresponding infinite horizontal layer, this convection

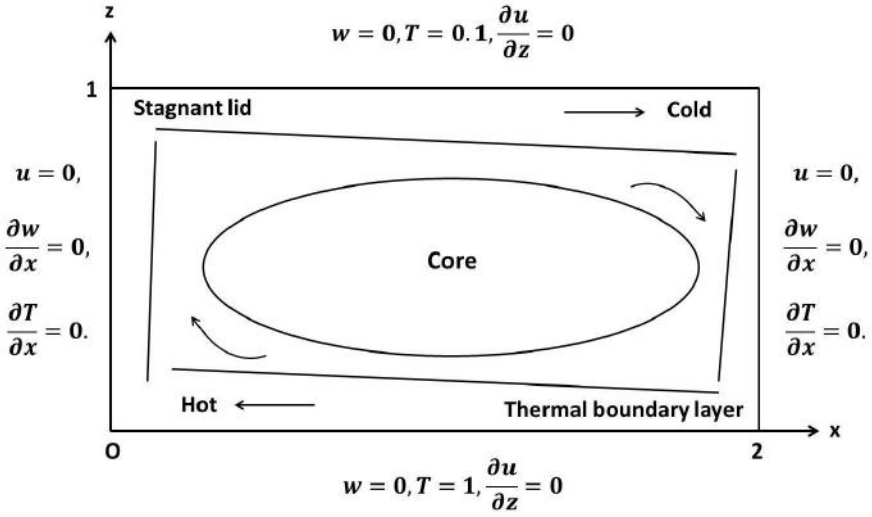

Figure 2.1: Schematic diagram of a basally heated elongated convection cell in mantle.

cell is regarded as a part of a periodic pattern.

The mass conservation can be represented by the incompressibility condition [6]. The inertial components in the Navier-Stokes equations are disregarded by considering an infinite Prandtl number appropriate for mantle convection [39]. As stated by Solomatov [40], the total mechanical work performed by thermal convection per unit of time usually balances the overall viscous dissipation inside the layer. If the difference in viscosity is significant, the dissipation occurring in the cold boundary layer can be similar to that observed in the internal region. Hence, we consider the "extended Boussinesq approximation" to balance the energy equation where the non-Boussinesq effect latent heat is taken into consideration and the fluid is regarded as incompressible throughout, with the exception of the propelling buoyancy forces. So, in the energy equation, we incorporate the non-Boussinesq effects of the frictional heating and adiabatic gradient [41]. Thus, conservation of mass, momentum, and energy along with the equation of state form

$$\frac{\partial \rho}{\partial t} + \nabla \cdot (\rho \boldsymbol{u}) = 0, \tag{2.1}$$

$$\nabla p = \nabla \cdot \boldsymbol{\tau} - \rho g \hat{k}, \tag{2.2}$$

$$\frac{\partial T}{\partial t} + \boldsymbol{u}.\nabla T - \frac{\alpha T}{\rho C_{\mathrm{p}}} \left(\frac{\partial P}{\partial t} + \boldsymbol{u}.\nabla P \right) = \kappa \left(\nabla^2 T \right) + \frac{\tau^2}{2\eta \rho C_{\mathrm{p}}}, \tag{2.3}$$

$$\rho = \rho_0 \left[1 - \alpha \left(T - T_b \right) \right]. \tag{2.4}$$

Here, $\boldsymbol{u} = (u, 0, w)$ represents the velocity of the fluid, where the component of velocity in the x- and z-directions are denoted by u and w, respectively, g stands for constant acceleration due to gravity (pointing downwards), η for viscosity and τ for the deviatoric stress tensor. Moreover, T stands for the absolute temperature, α for the thermal expansion coefficient, C_p for the specific heat at constant pressure, κ for the thermal diffusivity, ρ_0 for the basal density and T_b for the basal temperature, and P, t, ρ have their usual meaning. We assume that basal heating is the primary source of convection for our study and exclude internal heating and radiogenic heating.

The viscosity function in the Arrhenius form which relates temperature, pressure and stress dependency is considered in this study which is given by [42]

$$\eta = \frac{1}{2A^* \|\tau\|^{n-1}} \exp\left[\frac{E + pV}{RT} \right]. \tag{2.5}$$

Here, A^* stands for the pre-exponential factor; E for activation energy per mole; R for universal gas constant; and V for activation volume per mole. $\|\tau\|$ is the square root of the second invariant of the deviatoric stress tensor. Korenaga [43] investigates the superiority of Arrhenius rheology over linear-exponential rheology and

shows how well it can assess top thermal boundary layer stability.
The deviatoric stress tensor $\boldsymbol{\tau}$ can be representated as

$$\boldsymbol{\tau} = \eta \left[\nabla \boldsymbol{u} + (\nabla \boldsymbol{u})^T\right].$$

In this paper, Newtonian rheology with $n = 1$ is taken into consideration. Thus, the viscosity relation (2.5) can be reduced as

$$\eta = \frac{1}{2A^*} \exp\left[\frac{E + pV}{RT}\right]. \tag{2.6}$$

The boundary conditions
We take into consideration a rectangular convection cell of depth d that has a boundary condition of free-slip on all boundaries. We assume that the side walls are thermally insulated and the temperatures at the top and the bottom walls are constant. The boundary conditions for the model equations are

$$\begin{aligned} &w = 0, \quad T = T_\mathrm{b}, \quad \tau_3 = 0 \quad \text{on} \quad z = 0, \\ &w = 0, \quad T = T_\mathrm{s}, \quad \tau_3 = 0 \quad \text{on} \quad z = d, \\ &u = 0, \quad \frac{\partial T}{\partial x} = 0, \quad \tau_3 = 0 \quad \text{on} \quad x = 0, ad. \end{aligned} \tag{2.7}$$

Table 2.1: Relevant values of parameters for the mantle convection of the Earth.

Parameters	Symbols	Values
Basal temperature of the mantle	T_b	$3000K$
Temperature at the upper surface of the mantle	T_s	$300K$
Temperature difference	ΔT	$2700K$
Gravitational acceleration	g	$10\ ms^{-2}$
Reference density	ρ_0	$4 \times 10^3\ kgm^{-3}$
Mantle depth	d	$3 \times 10^6\ m$
Thermal conductivity	K	$4\ Wm^{-1}K^{-1}$
Thermal expansion coefficient	α	$2 \times 10^{-5}\ K^{-1}$
Thermal diffusivity	κ	$1 \times 10^{-6}\ m^2s^{-1}$
Specific heat at constant pressure	C_p	$10^3\ Jkg^{-1}K^{-1}$
Gas law constant	R	$8.31\ Jmol^{-1}K^{-1}$
Activation volume	V	$6 \times 10^{-6}\ m^3mol^{-1}$
Activation energy	E	$300 - 525\ kJmol^{-1}$
Viscous rate constant	A^*	$10^5\ MPa^{-1}s^{-1}$
Viscous pressure number	μ	$1.2 - 2.4$
Viscous temperature parameter	ϵ	$.042 - .083$
Dimensionless surface temperature	θ_0	0.1
Rayleigh number	Ra	$10^7 - 10^9$
Boussinesq number	$\bar{B}$	0.06

2.1 Dimensionless equations and parameters

We use the following dimensionless variables to non-dimensionalize the model equations and boundary conditions [44, 45]:

$$\begin{gathered} \boldsymbol{u} = \tfrac{\kappa}{d}\boldsymbol{u}^*, \quad t = \tfrac{d^2}{\kappa}t^*, \quad P = \rho_0 g d\,(1 - z^*) + \tfrac{\eta_0 \kappa}{d^2}P^*, \quad \rho = \rho_0 \rho^*, \quad \boldsymbol{\tau} = \tfrac{\eta_0 \kappa}{d^2}\boldsymbol{\tau}^*, \\ (x, z) = d\,(x^*, z^*), \quad \eta = \tfrac{e^{(1+\mu)/\varepsilon}}{2A^*}\eta^* = \eta_0 \eta^*, \quad T = T_\mathrm{b} T^*. \end{gathered} \tag{2.8}$$

This transformation produces the following dimensionless equations from equations (2.1), (2.2), (2.3), and (2.6):

$$\nabla \cdot \boldsymbol{u} = 0, \tag{2.9}$$

$$\nabla p = \nabla \cdot (\eta \nabla \boldsymbol{u}) - Ra(1 - T)k, \tag{2.10}$$

$$\frac{\partial T}{\partial t} + \boldsymbol{u} \cdot \nabla T + DTw - DT\frac{\bar{B}}{Ra}\frac{\partial P}{\partial t} - DT\frac{\bar{B}}{Ra}u \cdot \nabla P = \nabla^2 T + \frac{D}{Ra}\frac{\tau^2}{2\eta}, \tag{2.11}$$

$$\eta = \exp\left[\frac{(1-T)(1+\mu) + \mu\bar{B}p/Ra - \mu z}{\varepsilon T}\right]. \tag{2.12}$$

The dimensionless parameters appeared in the transformed equations form

$$\begin{aligned}
\text{Viscous temperature parameter, } \varepsilon &= \tfrac{RT_\mathrm{b}}{E},\\
\text{Boussinesq number, } \bar{B} &= \alpha T_\mathrm{b},\\
\text{Viscous pressure number, } \mu &= \tfrac{\rho_0 g\ \mathrm{d}V}{E},\\
\text{Rayleigh number, } Ra &= \tfrac{\alpha\rho_0 g T_\mathrm{b} d^3}{\eta_0 \kappa},\\
\text{Dissipation number, } D &= \tfrac{\alpha d g}{C_\mathrm{p}}.
\end{aligned} \tag{2.13}$$

From Table 2.1, we can see that $Ra \gg 1$ and so, $\frac{\bar{B}}{Ra} \ll 1$, and hence we can neglect this ratio. Then the non-dimensional equations (2.11) and (2.12) take the form as

$$\frac{\partial T}{\partial t} + \boldsymbol{u}\cdot\nabla T + DTw = \nabla^2 T + \frac{D}{Ra}\frac{\tau^2}{2\eta}, \tag{2.14}$$

$$\eta = \exp\left[\frac{(1+\mu)(1-T) - \mu z}{\varepsilon T}\right], \tag{2.15}$$

When the depth dependence, *i.e,* pressure dependence on viscosity function is neglected, the value of μ becomes 0. As a result, the constitutional relation (2.15) becomes

$$\eta = \exp\left[\frac{1-T}{\varepsilon T}\right], \tag{2.16}$$

where only temperature dependence is considered. The boundary conditions (2.7) in dimensionless form become

$$\begin{aligned}
&w = 0, \quad T = 1, \quad \tau_3 = 0 \quad \text{on} \quad z = 0,\\
&w = 0, \quad T = \frac{T_\mathrm{s}}{T_\mathrm{b}} = \theta_0, \quad \tau_3 = 0 \quad \text{on} \quad z = 1,\\
&u = 0, \quad \frac{\partial T}{\partial x} = 0, \quad \tau_3 = 0 \quad \text{on} \quad x = 0, a.
\end{aligned} \tag{2.17}$$

The dimensionless variable viscosity model includes the boundary conditions (2.17), with equations (2.9), (2.10), (2.14), and (2.15).

In our investigation, we ignore isothermal compressiblity, internal heating and radiogenic heating. Activation energy (E) is different in diffusion creep and in dislocation creep. That's why, the viscous temperature parameter (ϵ) and viscous pressure number (μ) are shown in a range in Table 2.1. It is very difficult to compute with the very small values of the viscous temperature parameter ϵ, and hence, we try to use the value of ϵ as small as possible. Similarly, with large viscous pressure number μ, the computation becomes very stiff. So, we try to choose a relatively high μ.

Next we define three indicative quantities that will be utilized in the findings in the next section.

i. Nusselt number

One way to quantify the heat transfer between a convective fluid and a surface is by looking at the Nusselt number. The Nusselt number, denoted by Nu, is a measure of the relative importance of convective and conduction-only heat flows on a given surface. The calculation of the Nusselt number is determined by the dimensionless relationship

$$\mathrm{Nu} = -\frac{1}{a\,(1-\theta_0)}\int_0^a \frac{\partial T}{\partial z}(x,1)\mathrm{d}x. \tag{2.18}$$

When it comes to conduction, the value of Nu is 1, but convection begins when it surpasses 1 [32].

ii. Root mean square velocity

The non-dimensional root mean square velocity V_{rms} is a measurement to accurately describe the strength of the flow that is circulating [21]. It is described as

$$V_{\text{rms}} = \left[\int_0^1 \int_0^a \left(u^2 + w^2\right) \mathrm{d}x \; \mathrm{d}z\right]^{1/2}. \tag{2.19}$$

Here, u represents the lateral velocity component and w represents the vertical velocity component.

iii. Viscosity variation

The viscosity variation, denoted by the symbol $\Delta\eta$, is defined as the numerical value that represents the ratio between the surface viscosity and the basal viscosity values. This contrast is defined as

$$\Delta\eta = \exp\left(\frac{1 - \theta_0 - \mu\theta_0}{\varepsilon\theta_0}\right). \tag{2.20}$$

3 Methodology

3.1 Process of computation

We perform our numerical computation by solving the dimensionless equations with a commercial software named 'COMSOL Multiphysics 6.1'. This software is a PDE solver which is based on finite element method. According to our model's physics, the modules named creeping flow, heat transfer in fluids and Poisson's equation are selected. For meshing technique, the "extra fine" for free triangular meshing options is chosen. Because of the boundary layers, in the vicinity of the boundaries of the cell, a refinement of 200 x 200 is applied.

Even though we are interested with high Rayleigh number convection with extreme viscosity contrast, COMSOL Multiphysics can not find a solution for $Ra = 10^7$ directly. For the convergence to a solution, Newton's method must start near a solution. For a nonlinear problem, the initial condition may not be in the 'basin of attraction' for the desired solution. That is why, we start by solving the system for a low Ra with relatively large value of ϵ and then restart the simulation with a slightly larger value of Ra but this time we use the solution of the low Ra convection as the initial condition. In this way, we gradually increase the value of Ra by using the solution of the previous simulation as the initial guess. When we achieve the solution of the high Ra convection, we decrease the value of temperature dependence parameter ϵ to increase the viscosity ratio across the layer. The process can be termed as the 'parametric continuation'. Because the solution at the new parameter values is not expected to be much different than at the old parameter values, the Newton solver should converge rapidly. We use implicit time-stepping method in time dependent solver and the MUMS solver for both stationary and time dependent solvers as these ensure the smooth convergence to the desired solutions.

3.2 Validation and Comparison

To validate our model, at first we simulate the mathematical model for constant viscosity in a square cell in the absence of viscous dissipation and internal heating. We set $\theta_0 = 0$ and $\eta = 1$ for this simulation. We compute the Nusselt number (Nu) and RMS velocity (V_{rms}) for Rayleigh number (Ra) 10^4 to 10^7. We compare these two values with the benchmark values given by Blankenbach et al. [27][a] and Koglin Jr et al. [46][b] in Table 3.1. From Table 3.1, it can be observed that the relative error is extremely minimal and it is less than 0.1% in all cases. This validates the construction of our model.

Table 3.1: Nusselt number and RMS velocity comparison with benchmarks.

Ra	**Nu**			$\boldsymbol{V}_{\text{rms}}$		
	This work	Benchmark	Error (%)	This work	Benchmark	Error (%)
10^4	4.884410	4.884409[a]	0.000017	42.864971	42.864947[a]	0.000056
10^5	10.534068	10.534095[a]	0.000256	193.214111	193.21454[a]	0.000222
10^6	21.972616	21.972465[a]	0.000688	834.004668	833.98977[a]	0.001786
10^7	45.639494	45.62[b]	0.042732	3633.893493	-	-

Table 3.2: Comparison of the computed Nu and V_{rms} values from convection with full form viscosity function with the values from convection with cut-off viscosity function [32] in a square cell with $D = 0.0$, $\mu = 0.0$ at $\theta_0 = 0.1, Ra = 10^7$.

μ	$\Delta\eta$	ϵ	**Nu**			$\boldsymbol{V}_{\text{rms}}$		
			This work	Previous work [32]	Error (%)	This work	Previous work [32]	Error (%)
	10^{10}	0.39	6.7623	6.76800	0.0842	752.8612	753.149	0.0382
	10^{15}	0.26	5.3573	5.36157	0.0796	594.7352	594.92	0.0311
0.0	10^{20}	0.195	4.4529	4.45036	0.0571	484.1178	483.396	0.1493
	10^{25}	0.156	3.8031	3.8009	0.0579	398.9110	398.149	0.1576
	10^{30}	0.1303	3.2594	3.25696	0.0749	309.2087	308.093	0.3621

Table 3.3: Comparison of the computed Nu and V_{rms} values from convection with full form viscosity function with the values from convection with cut-off viscosity function [32] in a square cell with $D = 0.3$ at different μ and $\theta_0 = 0.1, Ra = 10^7$.

μ	$\Delta\eta$	ϵ	**Nu**			$\boldsymbol{V}_{\text{rms}}$		
			This work	Previous work [32]	Error (%)	This work	Previous work [32]	Error (%)
	10^{10}	0.369	4.46509	4.46772	0.0589	580.132	580.307	0.0302
	10^{15}	0.246	3.62604	3.62823	0.0604	468.416	468.522	0.0226
0.5	10^{20}	0.1846	3.09281	3.09495	0.0691	388.036	388.104	0.0175
	10^{25}	0.1477	2.71437	2.71655	0.0802	324.924	324.978	0.0166
	10^{30}	0.123	2.40285	2.40512	0.0944	259.832	259.877	0.0173
	10^{10}	0.3474	5.22822	5.22977	0.0296	722.297	722.471	0.0241
	10^{15}	0.2316	4.58858	4.58926	0.0148	640.339	640.405	0.0103
1.0	10^{20}	0.1737	4.18630	4.18656	0.0062	563.067	562.901	0.0295
	10^{25}	0.1389	3.89039	3.88971	0.0175	482.400	481.827	0.1189
	10^{30}	0.1158	3.64316	3.64133	0.0503	399.355	398.414	0.2362

Next we show the comparison with a previous study for a convection model with temperature-dependent viscosity but without viscous dissipation effect ($D = 0.0$) in Table 3.2 and then, a comparison is shown for a convection model with temperature-and pressure- dependent viscosity and viscous dissipation effect ($D = 0.3$) in Table 3.3. It can be observed that the percentage error for the values of Nusselt number is less than 0.1% and for the values of root mean square velocity is less than 0.5%. It should be mentioned that in the reference paper [32], a cut-off viscosity function was employed for computational work. Hence, a slight difference is expected, but they still fall within an acceptable range. These comparisons further consolidate the robustness of our proposed model.

4 Result and Discussion

In our study, we employ the previously discussed model structure to a rectangular cell with two different aspect ratios: 2:1 (aspect ratio $a = 2$) and 1:2 (aspect ratio $a = 0.5$). We use the non-dimensional governing equations (2.9), (2.10), (2.14) and (2.15) with boundary conditions (2.17) for our simulation. The typical values of the parameters relevant to the Earth are given in Table I. These values suggest that the viscosity contrast across the mantle is of order 10^{50} or more. However, simulation with such high viscosity variation is computationally very expensive. Thus to tackle such computational complexity, in this study, we evaluate thermal convection at viscosity contrasts, $\Delta\eta$ up to 10^{30} at $Ra = 10^7$ mostly. According to Jarvis and Mckenzie [47], the value of D ranges from 0.25 to 0.8. Later, Leng and Zhong [29] claim the dissipation number to be in between 0.5 to 0.7. In this study, the numerical computations are carried out mainly for dissipation number

$D = 0.3 \sim 0.6$.

4.1 Convection with temperature-dependent viscosity $\eta(T)$

In this section, the results of elongated and narrow convection cells are presented, where the effect of the temperature-dependent viscosity ($\eta(T), \mu = 0$) is considered with viscous dissipation.

Table 4.1: Nusselt number (Nu) and root mean square velocity (V_{rms}) values from convection with $\eta(T)$ in elongated cell with aspect ratio $a = 2$ and narrow cell with aspect ratio $a = 0.5$ at $\theta_0 = 0.1$, $\mu = 0.0$ and $Ra = 10^7$.

$\Delta\eta$	ϵ	**Elongated Cell,** $a = 2$				**Narrow cell,** $a = 0.5$			
		Nu		V_{rms}		**Nu**		V_{rms}	
		$D = 0.3$	$D = 0.6$	$D = 0.3$	$D = 0.6$	$D = 0.3$	$D = 0.6$	$D = 0.3$	$D = 0.6$
10^5	0.782	4.4935	2.9161	686.804	490.439	6.8237	4.0386	483.756	319.061
10^{10}	0.39	3.0331	1.9570	470.797	306.056	4.4444	2.506	327.765	187.912
10^{15}	0.26	2.4181	1.5904	354.683	210.461	3.3037	1.8858	239.132	121.544
10^{20}	0.195	2.0426	1.3900	277.561	150.077	2.6414	1.5762	181.810	84.539
10^{25}	0.156	1.7888	1.2586	221.075	106.165	2.2156	1.3993	141.566	61.913
10^{30}	0.1303	1.6089	1.2510	177.696	91.560	1.9280	1.2906	112.285	47.300

Table 4.1 shows that in elongated cell as well as in narrow cell with temperature-dependent viscosity, for a certain dissipation number D, Nu and V_{rms} decrease with the increase of viscosity contrast. As the parameter $\Delta\eta$ is only temperature-dependent, these results imply that convection weakens with higher viscosity gradients across the mantle. Additionally, it can be observed that at a fixed viscosity contrast, the value of the Nusselt number and V_{rms} decrease as the dissipation number D increases from 0.3 to 0.6. So, stronger influence of D also weakens the convection.

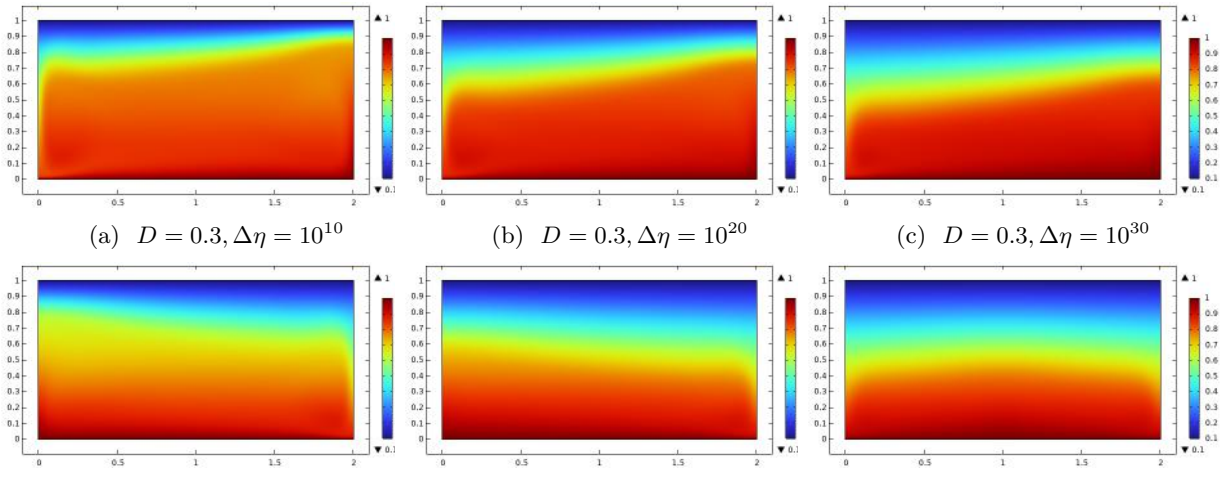

(a) $D = 0.3, \Delta\eta = 10^{10}$ (b) $D = 0.3, \Delta\eta = 10^{20}$ (c) $D = 0.3, \Delta\eta = 10^{30}$

(d) $D = 0.6, \Delta\eta = 10^{10}$ (e) $D = 0.6, \Delta\eta = 10^{20}$ (f) $D = 0.6, \Delta\eta = 10^{30}$

Figure 4.1: Temperature distribution in a 2:1 convection cell for different viscous dissipation number at various viscosity ratios $\Delta\eta$ with $\mu = 0.0$, $\theta_0 = 0.1$ and $Ra = 10^7$.

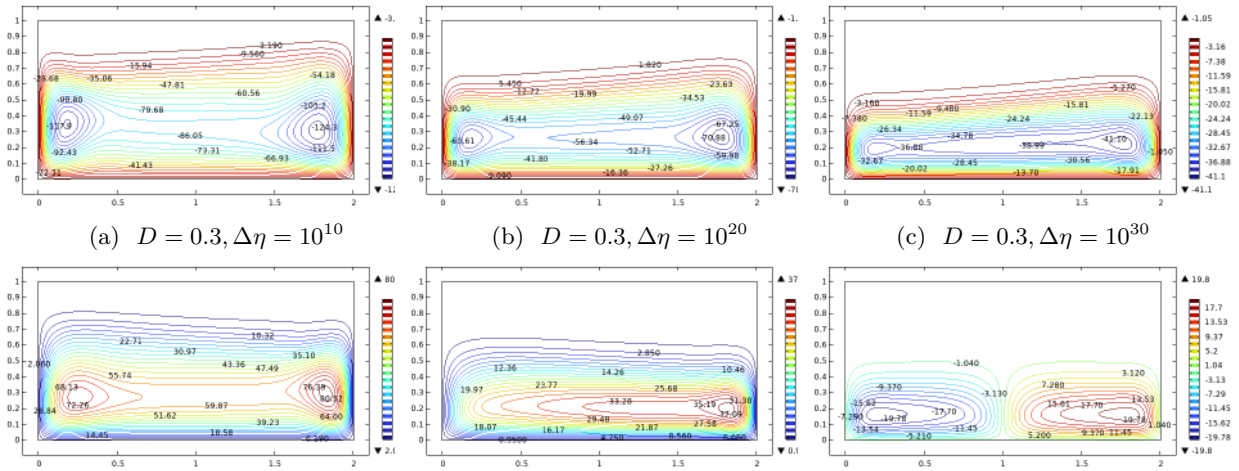

(a) $D = 0.3, \Delta\eta = 10^{10}$ (b) $D = 0.3, \Delta\eta = 10^{20}$ (c) $D = 0.3, \Delta\eta = 10^{30}$

(d) $D = 0.6, \Delta\eta = 10^{10}$ (e) $D = 0.6, \Delta\eta = 10^{20}$ (f) $D = 0.6, \Delta\eta = 10^{30}$

Figure 4.2: Stream function distribution in a 2:1 convection cell for different viscous dissipation number at various viscosity ratios $\Delta\eta$ with $\mu = 0.0$, $\theta_0 = 0.1$ and $Ra = 10^7$.

Figure 4.1 and 4.2 represent the temperature distribution and stream function contours, respectively at various viscosity contrasts ($\Delta\eta$) at different viscous dissipation numbers (D) with $\mu = 0.0$ in an elongated cell. Temperature profiles are shown in figure 4.1 where a cold and a hot thermal boundary layer at the top (blue) and at the bottom (red) of the cell, respectively are clearly visible. The fluid in the cold boundary layer develops a stiff lid because of high viscosity. Panels (4.1a-4.1c) for $D = 0.3$ and panels (4.1d-4.1f) for $D = 0.6$ illustrate a gradual increase of the blue region. It can be concluded that the lid grows thicker with the rise of the viscosity contrast. The blue area in panel 4.1f is greater than panel 4.1c, which means that the lid thickness becomes larger when the dissipation becomes stronger. It can also be seen from the figure that the temperature at the base of the cell continues to increase. The growing dark red area demonstrates this characteristics. So, the temperature is greater in the vicinity of the core-mantle boundary layer, and it increases as the viscosity contrast starts to increase.

In each panel of Figure 4.2, no streamlines can be found at the uppermost part of the convection cell. This confirms the existence of a stagnant lid at the top of the mantle. It can also be seen that as the viscosity gradient increases, a big portion at the upper part is free of streamlines. This also validates the growth of stagnant lid thickness. In addition to this, it can also be observed that at a specific dissipation number $D = 0.3$, the single cell convection pattern persists, regardless of the viscosity contrast. However, for $D = 0.6$, an obvious change in convection pattern is visible for larger viscosity gradients. When $\Delta\eta$ becomes 10^{30}, convection cell pattern becomes unstable, single cell disappears. Here unstable means that the stationary solver does not converge for this particular set of parameters. However, when the time-dependent solver is applied, the two-cell steady pattern emerges (panel 4.2f). This can happen when the new parameter is close to a bifurcation point - in which multiple solutions are possible. Therefore, for dissipation number $D = 0.6$, two square cell pattern is the stable choice when $\Delta\eta$ is high enough. The mechanism adapts to increase viscosity sensitivity to temperature by confining flow to progressively smaller convection cells.

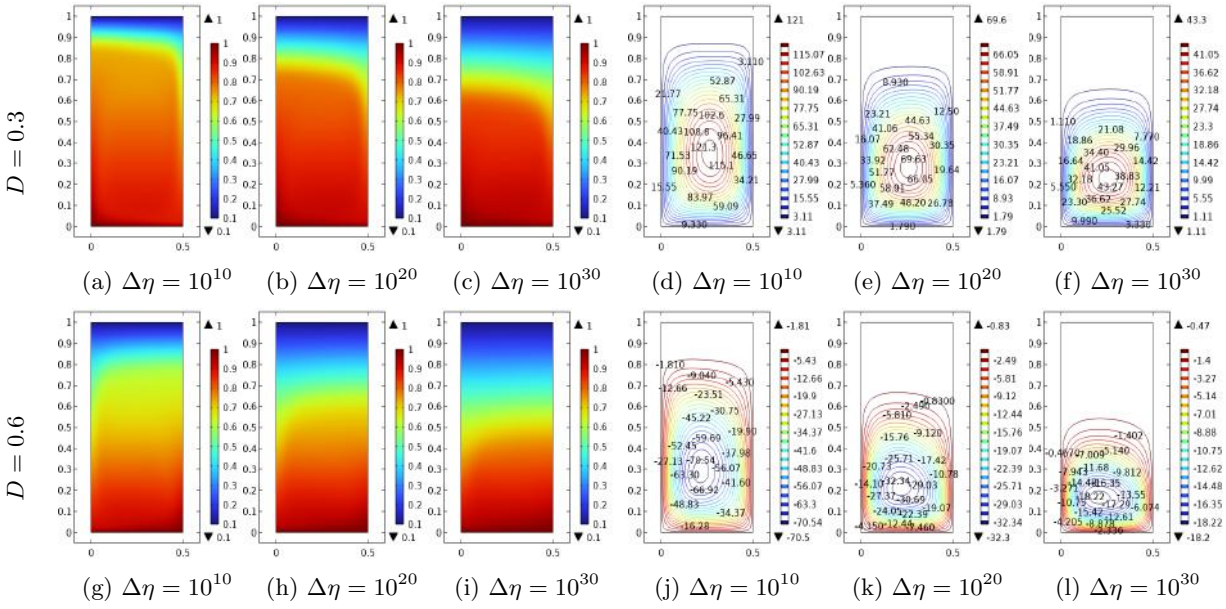

(a) $\Delta\eta = 10^{10}$ (b) $\Delta\eta = 10^{20}$ (c) $\Delta\eta = 10^{30}$ (d) $\Delta\eta = 10^{10}$ (e) $\Delta\eta = 10^{20}$ (f) $\Delta\eta = 10^{30}$

(g) $\Delta\eta = 10^{10}$ (h) $\Delta\eta = 10^{20}$ (i) $\Delta\eta = 10^{30}$ (j) $\Delta\eta = 10^{10}$ (k) $\Delta\eta = 10^{20}$ (l) $\Delta\eta = 10^{30}$

Figure 4.3: Temperature distribution with corresponding stream function distribution in a 1:2 convection cell for different viscous dissipation number at various viscosity ratios $\Delta\eta$ with $\mu = 0.0$, $\theta_0 = 0.1$ and $Ra = 10^7$.

For convection with $\eta(T)$ at different D and $\Delta\eta$, the temperature profiles and the streamlines in a narrow cell are presented in Figure 4.3. Like elongated cell, there is a gradual increase in cold blue zone and decrease of warm yellow zone as the viscosity gradient advances to higher values in the narrow cell. So, it can be concluded that when the viscosity variation becomes larger at a fixed dissipation number, the convection in the mantle of the Earth becomes less intense. Figure 4.3 shows that the single-cell pattern of 1:2 narrow convection cell with $\eta(T)$ remains stable even at higher values of D and $\Delta\eta$.

The horizontally average temperature distribution as a function of depth is presented in Figure 4.4. The horizontally average temperature at mid-depth [48] is defined as

$$\bar{T}_{z=d/2} = \frac{1}{a}\int_0^a T(x, z = d/2)dx \tag{4.1}$$

where z represents the depth of the cell.

The Figures 4.4a and 4.4b show that the increase of viscous dissipation number and viscosity contrast lead to lower horizontally averaged temperature $\bar{T}$ in the mantle. From the figures, it can be seen that the narrow cell has higher $\bar{T}$ than the elongated cell. It can be inferred from the plots that the interior of the mantle is not isothermal. When the dissipation number is higher ($D = 0.6$), implying a greater dissipation effect, the inside of both types of cells experience a significant temperature difference. For $D = 0.3$, there is a remarkable difference in the average temperature between the lid region and core of the mantle. However, for $D = 0.6$, the difference in the two regions is not that distinguishable. It is also evident that the hot thermal boundary layer at the bottom is significantly thinner than the cold upper boundary layer.

Figure 4.5 shows the variation of Nu with Ra for different values of ϵ in different aspect ratio convection cells. At a fixed ϵ, as Ra increases from 10^6 to 10^8, the value of Nu also increases and this indicates that stronger convection occurs in the mantle. This trend can be seen for different values of D and in both elongated and narrow cells. At a certain D in both cells, as ϵ decreases, i.e. $\Delta\eta$ becomes larger, Nu decreases and the convection becomes weaker. Also Nu values decrease as dissipation gets stronger which implies viscous dissipation dampens heat transfer efficiency in the mantle convection.

4.2 Convection with temperature-and pressure-dependent viscosity $\eta(T, z)$

In this section, the simulation results for convection with temperature- and pressure-dependent viscosity $\eta(T, z)$ will be analyzed. For viscous pressure number, $\mu = 0.5$ and $\mu = 1$, Nu and V_{rms} values along with the thermal distributions and corresponding streamlines are presented in this section in Figures 4.6 - 4.9. Here, we vary $\Delta\eta$ and dissipation number D to find their effect on convection cells with aspect ratio $a = 2$ and $a = 0.5$.

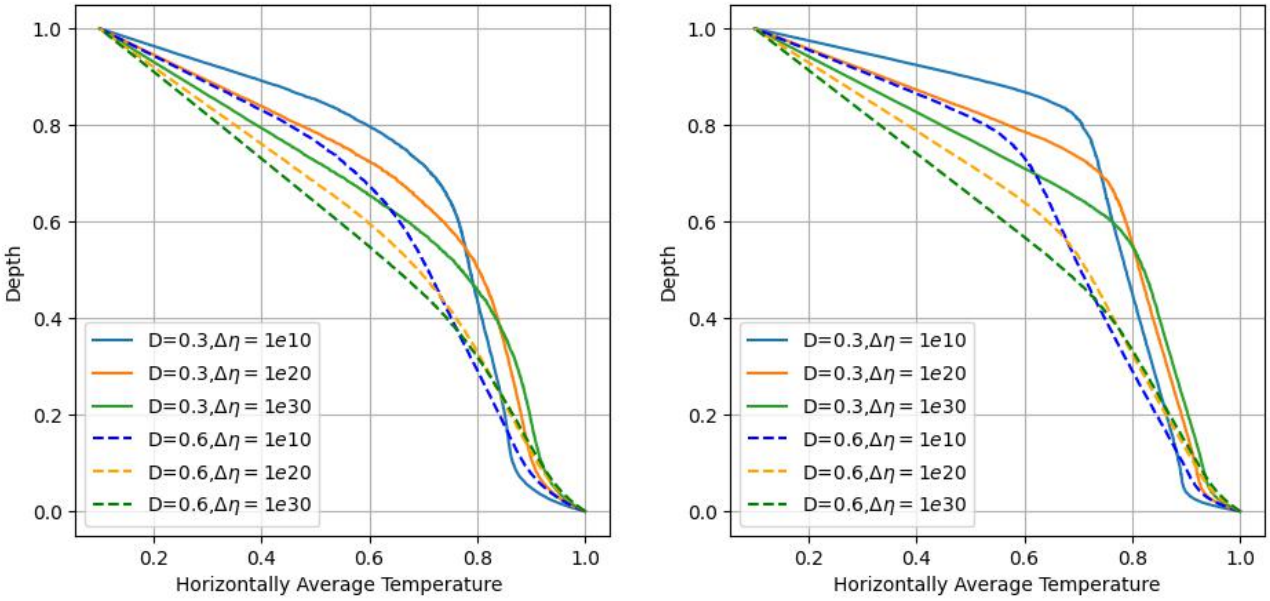

(a) Elongated cell (2:1)

(b) Narrow cell (1:2)

Figure 4.4: Horizontally average temperature $\bar{T}$ for different viscosity contrasts at various viscous dissipation numbers in two convection cells with $\eta(T)$ ($\mu = 0.0, \theta_0 = 0.1$, and $Ra = 10^7$).

Table 4.2: Nusselt number (Nu) and root mean square velocity (V_{rms}) values from convection with $\eta(T, z)$ in elongated and narrow cell at $\theta_0 = 0.1$, and $Ra = 10^7$.

μ	$\Delta\eta$	ϵ	**Elongated Cell,** $a = 2$				**Narrow cell,** $a = 0.5$			
			Nu		V_{rms}		Nu		V_{rms}	
			$D = 0.3$	$D = 0.5$	$D = 0.3$	$D = 0.5$	$D = 0.3$	$D = 0.6$	$D = 0.3$	$D = 0.6$
	10^5	0.738	4.7358	3.5341	757.931	601.606	7.3822	4.3119	544.169	349.314
	10^{10}	0.369	3.4219	2.4753	575.561	423.356	5.278	2.8259	423.828	232.024
0.5	10^{15}	0.246	2.8527	2.0246	469.830	320.062	4.2315	2.1531	352.775	162.886
	10^{20}	0.185	2.4872	1.7473	396.497	249.054	3.5754	1.7797	302.795	118.478
	10^{25}	0.148	2.2293	1.5605	342.826	196.777	3.1194	1.5518	264.484	88.445
	10^{30}	0.123	2.0353	1.4269	301.813	155.974	2.7804	1.4040	233.437	67.523
	10^5	0.694	4.9572	3.6748	839.444	666.174	7.9117	4.5695	611.358	393.232
	10^{10}	0.3474	3.8896	2.7486	710.808	517.712	6.2000	3.2178	520.312	293.266
1.0	10^{15}	0.2316	3.4532	2.3411	629.831	424.274	5.3823	2.5589	457.351	229.682
	10^{20}	0.1737	3.1914	2.0821	572.421	359.411	4.8657	2.1534	398.424	183.891
	10^{25}	0.1389	3.0230	1.8988	539.997	312.672	4.4749	1.8750	337.149	148.350
	10^{30}	0.1158	2.9041	1.7601	531.394	277.046	4.1354	1.6733	274.042	119.746

From Table 4.2, we observe that at a specific value of D, there is a decrease in the value of Nu and V_{rms} with the increase of viscosity ratio $\Delta\eta$ in the elongated cell as well as in the narrow cell for both $\mu = 0.5$ and $\mu = 1.0$. Again, it shows that at a particular $\Delta\eta$, Nu and V_{rms} decrease as D is increased. This provides the evidence that higher dissipation effect and viscosity contrast weaken the strength of the temperature- and

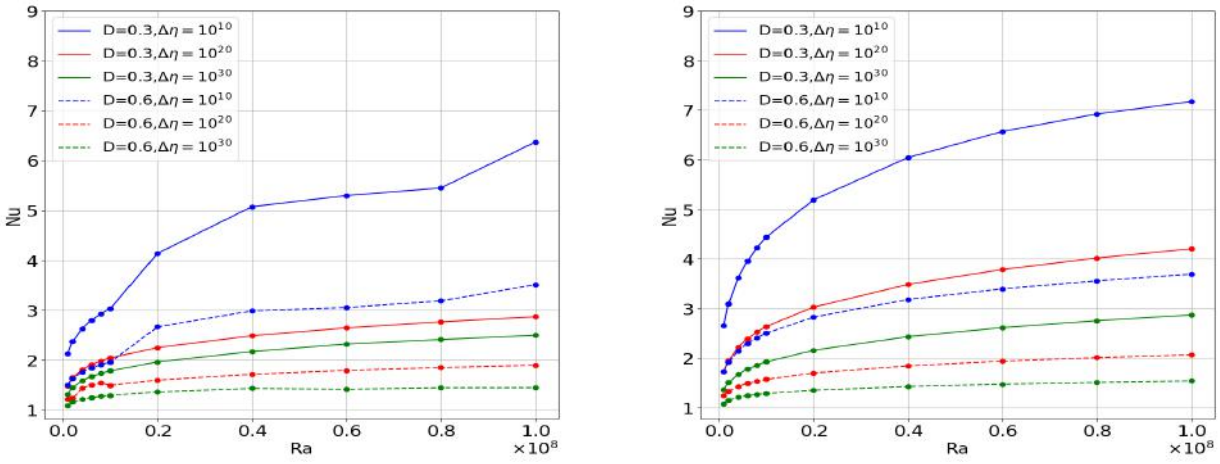

(a) Elongated cell (2:1) (b) Narrow cell (1:2)

Figure 4.5: Rayleigh vs Nusselt number plot for different viscosity contrasts with different viscous dissipation number in different convection cells ($\mu = 0.0, \theta_0 = 0.1$, and $Ra = 10^7$).

pressure-dependent viscous convection in both types of cells considered. However, at a fixed viscosity contrast, Nu and V_{rms} values increase as μ changes from 0.5 to 1.0. This implies stronger influence of pressure in the viscosity function boosts the convection vigour as viscous temperature parameter ϵ decreases.

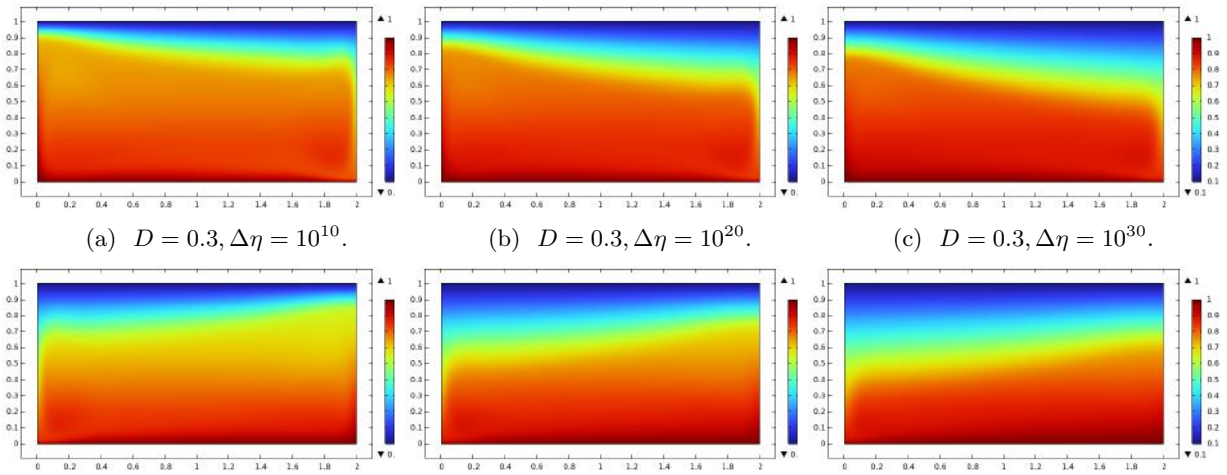

(a) $D = 0.3, \Delta\eta = 10^{10}$. (b) $D = 0.3, \Delta\eta = 10^{20}$. (c) $D = 0.3, \Delta\eta = 10^{30}$.

(d) $D = 0.5, \Delta\eta = 10^{10}$. (e) $D = 0.5, \Delta\eta = 10^{20}$. (f) $D = 0.5, \Delta\eta = 10^{30}$.

Figure 4.6: Thermal distributions in a 2:1 convection cell for different viscous dissipation number ($D = 0.3, 0.5$) at various viscosity ratios ($\Delta\eta = 10^{10}, 10^{20}, 10^{30}$) with $\mu = 0.5$, $\theta_0 = 0.1$ and $Ra = 10^7$.

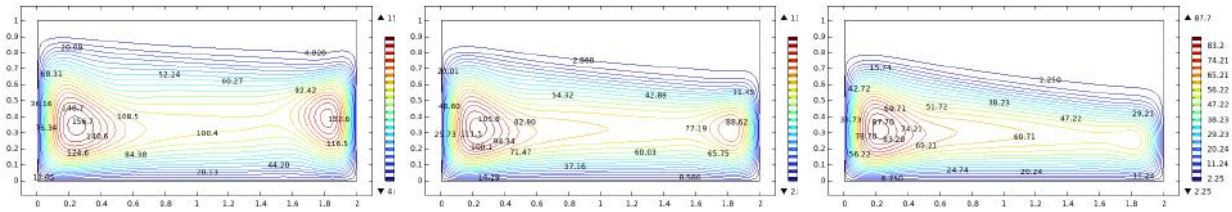

(a) $D = 0.3, \Delta\eta = 10^{10}$. (b) $D = 0.3, \Delta\eta = 10^{20}$. (c) $D = 0.3, \Delta\eta = 10^{30}$.

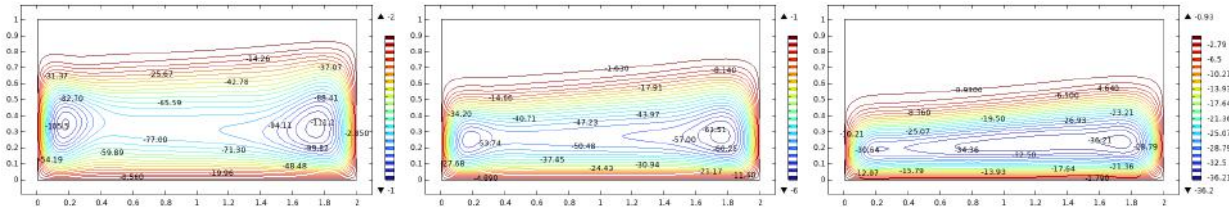

(d) $D = 0.5, \Delta\eta = 10^{10}$. (e) $D = 0.5, \Delta\eta = 10^{20}$. (f) $D = 0.5, \Delta\eta = 10^{30}$.

Figure 4.7: Stream function contours in a 2:1 convection cell for different viscous dissipation number ($D = 0.3, 0.5$) at various viscosity ratios ($\Delta\eta = 10^{10}, 10^{20}, 10^{30}$) with $\mu = 0.5$, $\theta_0 = 0.1$ and $Ra = 10^7$.

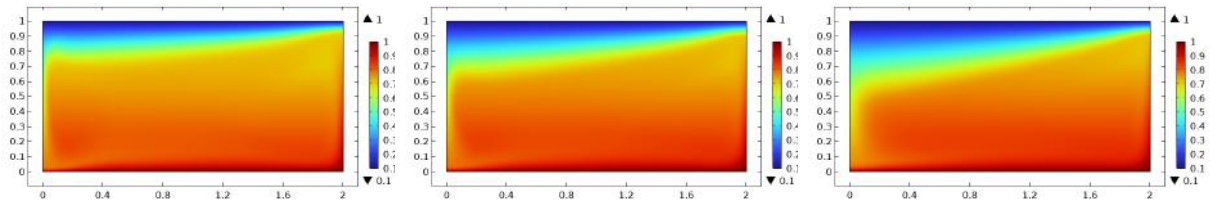

(a) $D = 0.3, \Delta\eta = 10^{10}$. (b) $D = 0.3, \Delta\eta = 10^{20}$. (c) $D = 0.3, \Delta\eta = 10^{30}$

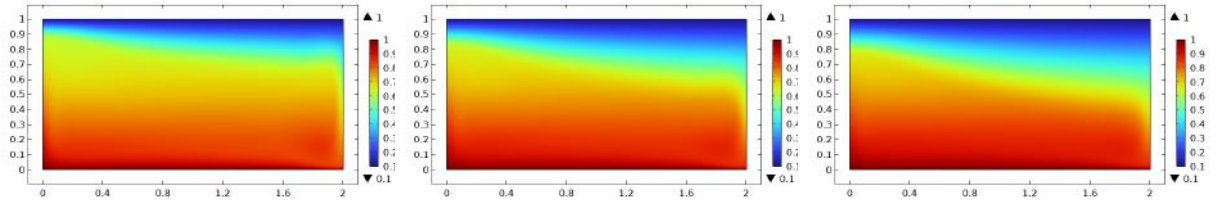

(d) $D = 0.5, \Delta\eta = 10^{10}$. (e) $D = 0.5, \Delta\eta = 10^{20}$. (f) $D = 0.5, \Delta\eta = 10^{30}$.

Figure 4.8: Thermal distributions in a 2:1 convection cell for different viscous dissipation number ($D = 0.3, 0.5$) at various viscosity ratios ($\Delta\eta = 10^{10}, 10^{20}, 10^{30}$) with $\mu = 1.0$, $\theta_0 = 0.1$ and $Ra = 10^7$.

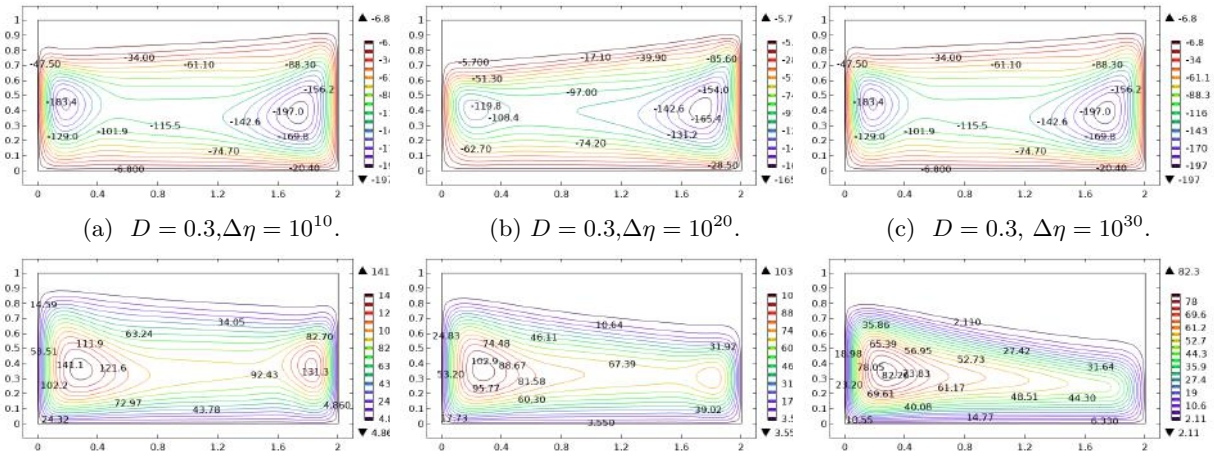

(a) $D = 0.3, \Delta\eta = 10^{10}$. (b) $D = 0.3, \Delta\eta = 10^{20}$. (c) $D = 0.3,\ \Delta\eta = 10^{30}$.

(d) $D = 0.5,\ \Delta\eta = 10^{10}$. (e) $D = 0.5, \Delta\eta = 10^{20}$. (f) $D = 0.5, \Delta\eta = 10^{30}$.

Figure 4.9: Stream function contours in a 2:1 convection cell for different viscous dissipation number ($D = 0.3, 0.5$) at various viscosity ratios ($\Delta\eta = 10^{10}, 10^{20}, 10^{30}$) with $\mu = 1.0$, $\theta_0 = 0.1$ and $Ra = 10^7$.

In Figures 4.6 - 4.9, the temperature distributions and streamfunction contours in a 2:1 elongated cell are displayed at two different viscous pressure numbers $\mu = 0.5$ and $\mu = 1.0$ for convection with $\eta(T, z)$. In each of Figures 4.6 to 4.9, thermal distributions and streamlines at various viscosity ratios ($\Delta\eta = 10^{10}, 10^{20}, 10^{30}$) and dissipation numbers ($D = 0.3, 0.5$) are showed. We observe that the blue zone progressively rises in both figure 4.6 and 4.8, which is the indicator of the increase of the cold area in the mantle as viscosity variation gets larger. The cold boundary layer thickness, that is, the stagnant lid thickness, is higher for $D = 0.5$ than $D = 0.3$ for both values of μ (Figures 4.6d, 4.6e, 4.6f and 4.8d, 4.8e, 4.8f). The orange region in the convection cell starts to shrink as $\Delta\eta$ becomes higher, and at the same time, the dark red area begins to occupy more and more area at the bottom of the cell. This outcome of the simulation suggests an increase in temperature in the lower mantle which is also similar to the Figure 4.2 where the value of μ was 0.0.

Stream function contours for $\mu = 0.5$ and $\mu = 1.0$ are shown in Figures 4.7 and 4.9, respectively. An increasing empty area at the top of the cell can be seen as $\Delta\eta$ becomes larger. We can also observe from these streamlines that single-cell pattern remains stable in a 2:1 convection cell even if the viscous pressure number μ, dissipation effect D, and viscosity ratio $\Delta\eta$ are increased significantly.

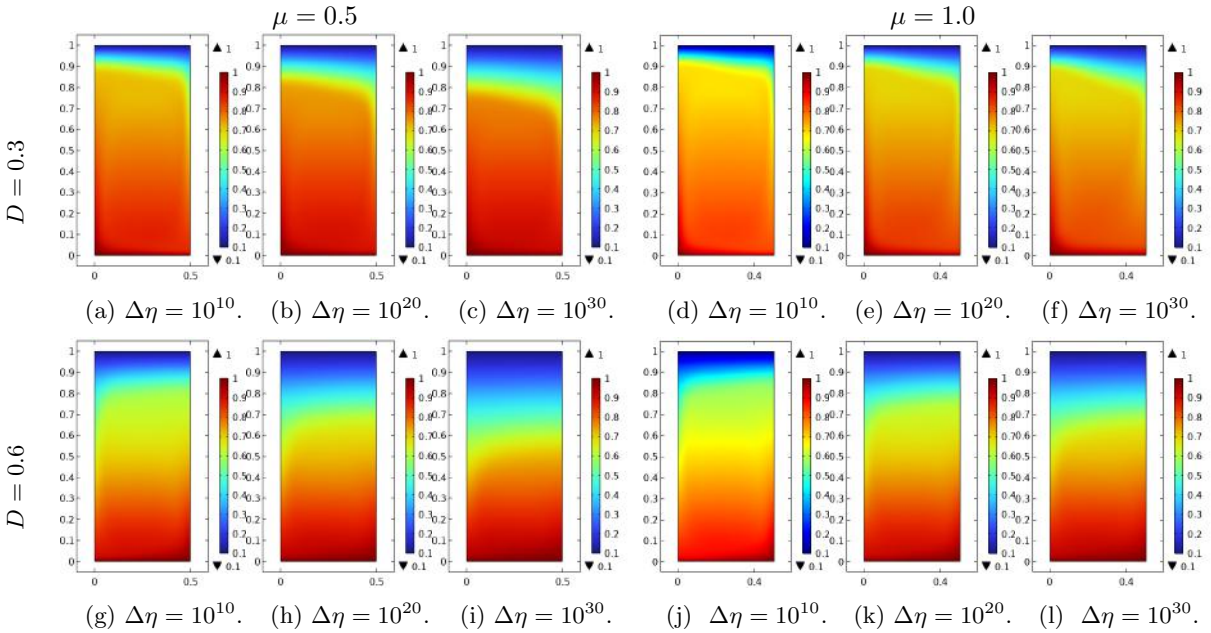

(a) $\Delta\eta = 10^{10}$. (b) $\Delta\eta = 10^{20}$. (c) $\Delta\eta = 10^{30}$. (d) $\Delta\eta = 10^{10}$. (e) $\Delta\eta = 10^{20}$. (f) $\Delta\eta = 10^{30}$.

(g) $\Delta\eta = 10^{10}$. (h) $\Delta\eta = 10^{20}$. (i) $\Delta\eta = 10^{30}$. (j) $\Delta\eta = 10^{10}$. (k) $\Delta\eta = 10^{20}$. (l) $\Delta\eta = 10^{30}$.

Figure 4.10: Temperature distribution in a 1:2 convection cell for different viscous dissipation number D and viscous pressure number μ at various viscosity ratios $\Delta\eta$ with $\theta_0 = 0.1$ and $Ra = 10^7$.

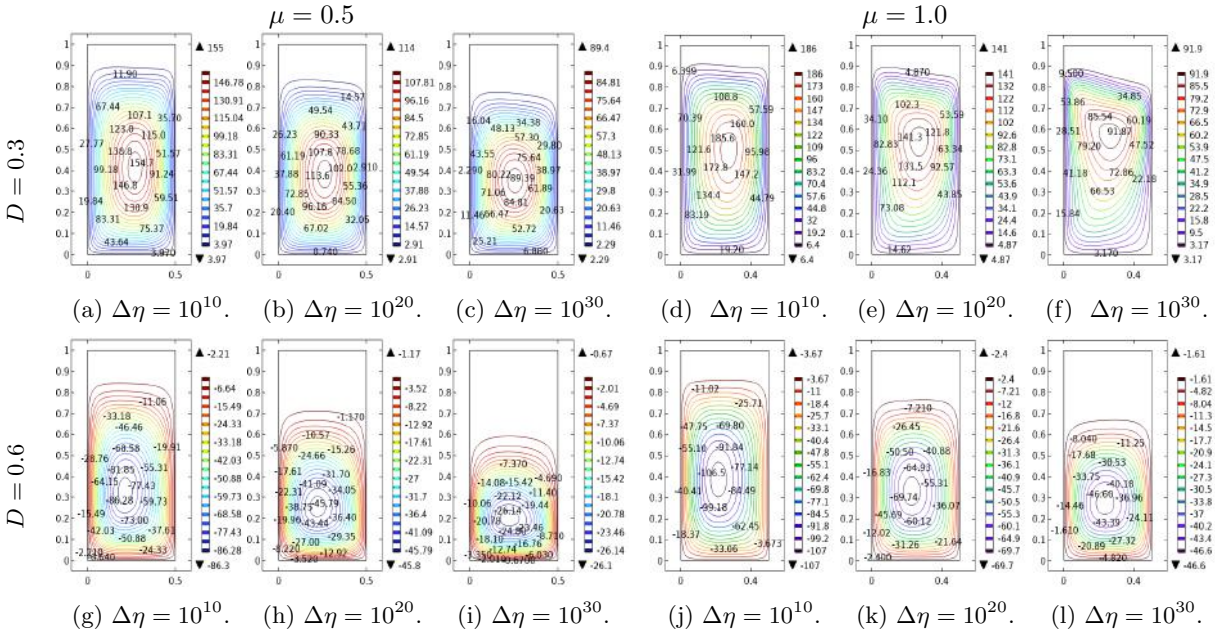

(a) $\Delta\eta = 10^{10}$. (b) $\Delta\eta = 10^{20}$. (c) $\Delta\eta = 10^{30}$. (d) $\Delta\eta = 10^{10}$. (e) $\Delta\eta = 10^{20}$. (f) $\Delta\eta = 10^{30}$.

(g) $\Delta\eta = 10^{10}$. (h) $\Delta\eta = 10^{20}$. (i) $\Delta\eta = 10^{30}$. (j) $\Delta\eta = 10^{10}$. (k) $\Delta\eta = 10^{20}$. (l) $\Delta\eta = 10^{30}$.

Figure 4.11: Stream function distribution in a 1:2 convection cell for different viscous dissipation number D and viscous pressure number μ at various viscosity ratios $\Delta\eta$ with $\theta_0 = 0.1$ and $Ra = 10^7$.

Next the temperature and stream function distributions for convection with $\eta(T, z)$ for $\mu = 0.5$ and $\mu = 1.0$ in a 1:2 narrow convection cell are presented in Figures 4.10, 4.11. There is a significant change in temperature in the interior of the convection cell. For $D = 0.3$, the interior temperature decreases significantly when μ is increased from 0.5 to 1.0 (Figure 4.10 a-f). The stagnant lid thickness increases with the increase of viscosity variation and dissipation number. Overall, the figures show a similar pattern in temperature and streamline as we observed in an elongated cell. A stable one-cell convection pattern persists in a narrow cell with temperature- and pressure-dependent viscosity at higher D and $\Delta\eta$.

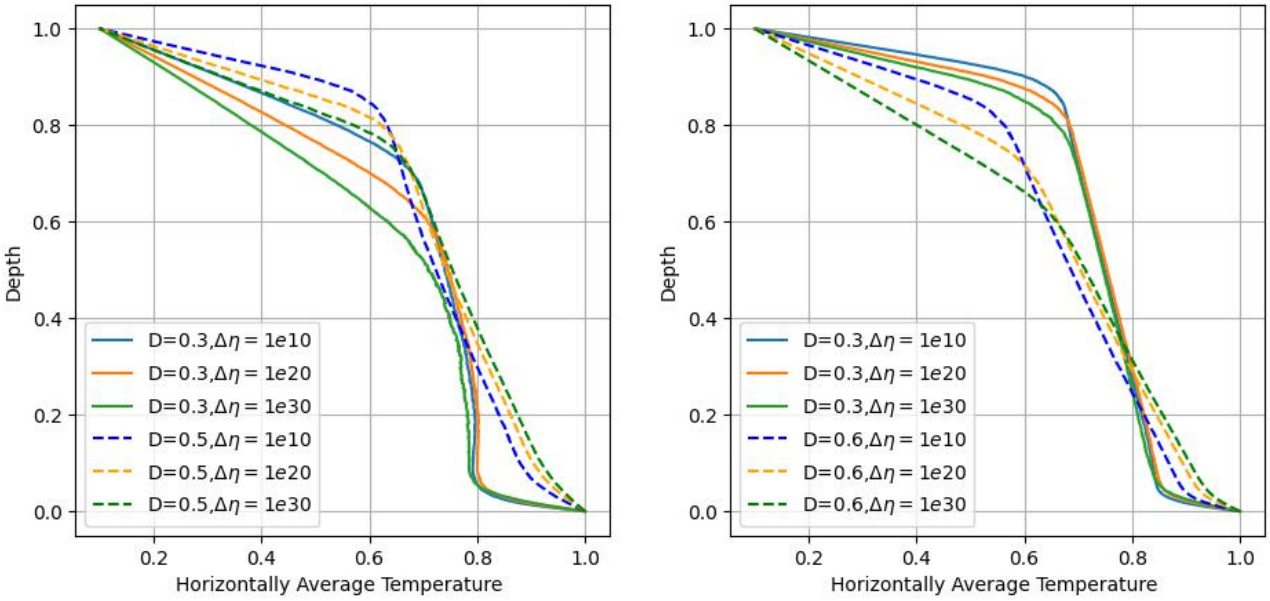

(a) Elongated cell (2:1) (b) Narrow cell (1:2)

Figure 4.12: Horizontally average temperature $\bar{T}$ for different viscosity contrasts at various viscous dissipation numbers in two convection cells with $\eta(T, z)$ ($\mu = 1.0, \theta_0 = 0.1$ and $Ra = 10^7$).

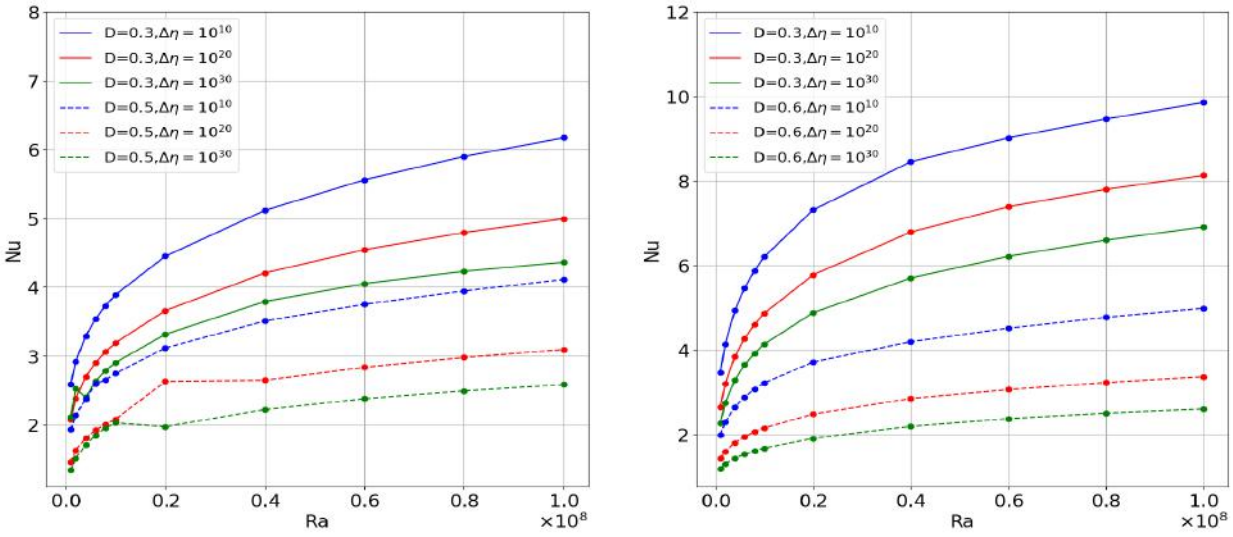

(a) Elongated cell (2:1) (b) Narrow cell (1:2)

Figure 4.13: Rayleigh vs Nusselt number plot for different viscosity contrasts with different viscous dissipation number in different convection cells at $\mu = 1.0, \theta_0 = 0.1$, and $Ra = 10^7$.

In Figure 4.12 horizontally average temperature profiles are displayed for both elongated and narrow cell for viscous pressure number $\mu = 1.0$. The most significant difference that can be seen is the increase of horizontally average temperature $\bar{T}$ as dissipation number D is increased from 0.3 to 0.5 in the elongated cell. Previously for temperature-dependent viscosity case ($\eta(T), \mu = 0.0$), $\bar{T}$ decreased as D is increased. The only exception is found in the case for elongated cell with $\eta(T, z), \mu = 1.0$. The narrow cell for $\eta(T, z)$ with $\mu = 1.0$ shows a similar trend like Figure 4.4b. As the temperature gradient is high in the boundary layers, this figure reveals that the cold upper thermal boundary layer in the elongated cell is much more thicker than in the narrow cell. Also for $D = 0.3$, the hot thermal boundary layer is quite prominent in both cells.

The Nu vs Ra plots for elongated and narrow convection cells at $\mu = 1.0$ are shown in Figure 4.13. From this figure a similar conclusion can be drawn as we did earlier from Figure 4.5.

5 Conclusion

The main purpose of this paper is to study the thermal convection in the mantle with significant temperature-dependent viscosity $\eta(T)$ and temperature and pressure-dependent viscosity $\eta(T, z)$ under the effects of viscous dissipation at a high Rayleigh number in basally heated convection cells of particular aspect ratios of 2:1 (elongated cell) and 1:2 (narrow cell). The simulation results are presented through thermal distribution and stream function contours. The heat transfer efficiency and vigour of convective motion are estimated by the Nusselt Number Nu and root mean square velocity V_{rms}, respectively. This study reveals that

- Nu and V_{rms} values decrease with the increase of dissipation number D and viscosity ratio $\Delta\eta$ for both convection with $\eta(T)$ and convection with $\eta(T, z)$ in different aspect ratio cells.
- Nu and V_{rms} values increase with the increase of viscous pressure number μ.
- In the elongated (aspect ratio 2:1) cell and the narrow (aspect ratio 1:2) cell a stable single-cell pattern persists at a high viscosity contrast at different dissipation numbers in both types of viscous convection. However, for $D = 0.6$ and $\mu = 0.0$ in an elongated cell, a tendency of cell break is observed at $\Delta\eta = 10^{30}$.
- In both aspect ratio cells, with the increase in dissipation number and viscosity contrasts, the rigid lid thickness at the top of the mantle increases, and the convection in the mantle becomes weaker.
- From the figures, it can be noted that in both elongated and narrow cells, the fluid is neither isothermal nor isoviscous.
- The Nu vs. Ra plots indicate that the strength of the convection in both types of convection cells with $\eta(T)$ and $\eta(T, z)$ weakens at higher Ra, D and $\Delta\eta$.

In this study, we investigated convection with very high viscosity contrast. It is mentioned that the usual parameters suggest that the viscosity ratio for the Earth's mantle is 10^{50} or more. Similarly, the viscosity ratio is of order 10^{20} for Venus and 10^{50} or more for Mars according to the relevant parameter values. Without extreme viscosity contrasts, it is quite impossible to obtain a proper asymptotic structure of mantle convection for the Earth and other terrestrial planets. Thus, it is believed that the analysis of the convection cells in this study will provide important clues for deciphering the dynamics of the Earth's interior and other similar planets with strong variable viscosity and high viscosity contrasts.

Acknowledgements

Noushin A. Trina would like to thank the support of National Science and Technology (NST) Fellowship.

Authors' contributions

The authors declare that the study was realized in collaboration with equal responsibilities. All the authors read and approved the final manuscript.

CRediT authorship contribution statement

Tania S. Khaleque: Writing, Data analysis, Conceptualization, Supervision, Project administration. **Noushin A. Trina:** Writing, Methodology, Validation, Investigation. **Sumaiya B. Islam:** Methodology, Validation, Investigation.

References

[1] National Research Council. *Origin and Evolution of Earth: Research Questions for a Changing Planet*. The National Academies Press, Washington, DC, 2008.

[2] Gerald Schubert, Donald Lawson Turcotte, and Peter Olson. *Mantle convection in the Earth and planets*. Cambridge University Press, 2001.

[3] Arthur Holmes. Radioactivity and Earth movements 1931. *Nature*, 128(3227), 1931.

[4] Arthur Holmes. The thermal history of the earth. *Journal of the Washington Academy of Sciences*, 23(4):169–195, 1933.

[5] Elvira Mulyukova and David Bercovici. Mantle convection in terrestrial planets. *Oxford Research Encyclopedia of Planetary Science*, 03 2020.

[6] Andrew Fowler. *Mathematical Geoscience*. 2011.

[7] Yawen She and Guangyu Fu. Viscosities of the crust and upper mantle constrained by three-dimensional gps rates in the sichuan–yunnan fragment of china. *Earth Planets and Space*, 71(1), 2019.

[8] DL Turcotte and ER Oxburgh. Finite amplitude convective cells and continental drift. *Journal of Fluid Mechanics*, 28(1):29–42, 1967.

[9] L-N Moresi and VS Solomatov. Numerical investigation of 2D convection with extremely large viscosity variations. *Physics of Fluids*, 7(9):2154–2162, 1995.

[10] Masanori Kameyama and Masaki Ogawa. Transitions in thermal convection with strongly temperature-dependent viscosity in a wide box. *Earth and Planetary Science Letters*, 180(3-4):355–367, 2000.

[11] Paul J Tackley. Self-consistent generation of tectonic plates in three-dimensional mantle convection. *Earth and Planetary Science Letters*, 157(1-2):9–22, 1998.

[12] Michael Gurnis and Geoffrey F Davies. The effect of depth-dependent viscosity on convective mixing in the mantle and the possible survival of primitive mantle. *Geophysical Research Letters*, 13(6):541–544, 1986.

[13] Tine B Larsen, Andrei V Malevsky, David A Yuen, and Jamie L Smedsmo. Temperature-dependent newtonian and non-newtonian convection: Implications for lithospheric processes. *Geophysical research letters*, 20(23):2595–2598, 1993.

[14] Chhavi Jain and Viatcheslav S Solomatov. How far below the critical rayleigh number can convection occur in temperature-dependent viscosity fluids? *Physics of the Earth and Planetary Interiors*, 329:106905, 2022.

[15] Chhavi Jain and VS Solomatov. Onset of convection in internally heated fluids with strongly temperature-dependent viscosity. *Physics of Fluids*, 34(9), 2022.

[16] Meysam Shahraki and Harro Schmeling. Plume-induced geoid anomalies from 2D axi-symmetric temperature- and pressure-dependent mantle convection models. *Journal of Geodynamics*, 59-60:193–206, 2012. Mass Transport and Mass Distribution in the System Earth.

[17] Rene Gassmöller, Juliane Dannberg, Wolfgang Bangerth, Timo Heister, and Robert Myhill. On formulations of compressible mantle convection. *Geophysical Journal International*, 221(2):1264–1280, 2020.

[18] Roberto Agrusta, A Morison, Stéphane Labrosse, R Deguen, T Alboussière, PJ Tackley, and F Dubuffet. Mantle convection interacting with magma oceans. *Geophysical Journal International*, 220(3):1878–1892, 2020.

[19] Tania S. Khaleque and S. A. Sayeed Motaleb. Effects of temperature- and pressure-dependent viscosity and internal heating on mantle convection. *GEM - International Journal on Geomathematics*, 12(1), 2021.

[20] Siddhant Agarwal, Nicola Tosi, Pan Kessel, Doris Breuer, and Grégoire Montavon. Deep learning for surrogate modeling of two-dimensional mantle convection. *Physical Review Fluids*, 6(11):113801, 2021.

[21] Tania S Khaleque, A C Fowler, Peter Howell, and Michael Vynnycky. Numerical studies of thermal convection with temperature- and pressure-dependent viscosity at extreme viscosity contrasts. *Physics of Fluids*, 27, 07 2015.

[22] Fabio A Capitanio, Oliver Nebel, Jean-François Moyen, and Peter A Cawood. craton formation in early earth mantle convection regimes. *Journal of Geophysical Research: Solid Earth*, 127(4):e2021JB023911, 2022.

[23] JA Whitehead. Convection cells with accumulating crust: Models of continent & mantle evolution. *Journal of Geophysical Research: Solid Earth*, page e2022JB025643, 2023.

[24] Masanori Kameyama. Linear analysis on the onset of thermal convection of highly compressible fluids with variable viscosity and thermal conductivity in spherical geometry: implications for the mantle convection of super-earths. *Earth, Planets and Space*, 73:1–17, 2021.

[25] Hisashi Okuda and Shin-ichi Takehiro. Horizontal length of finite-amplitude thermal convection cells with temperature-dependent viscosity. *Physics of the Earth and Planetary Interiors*, 344:107103, 2023.

[26] Sean James Trim, Samuel L Butler, Shawn SC McAdam, and Raymond J Spiteri. Manufacturing an exact solution for 2d thermochemical mantle convection models. *Geochemistry, Geophysics, Geosystems*, 24(4):e2022GC010807, 2023.

[27] B. Blankenbach, F. Busse, U. Christensen, L. Cserepes, D. Gunkel, U. Hansen, H. Harder, G. Jarvis, M. Koch, G. Marquart, D. Moore, P. Olson, H. Schmeling, and T. Schnaubelt. A benchmark comparison for mantle convection codes. *Geophysical Journal International*, 98(1):23–38, 07 1989.

[28] S J Trim, S L Butler, and Raymond J Spiteri. Benchmarking multiphysics software for mantle convection. *Computers & Geosciences*, 154:104797–104797, 09 2021.

[29] Wei Leng and Shijie Zhong. Constraints on viscous dissipation of plate bending from compressible mantle convection. *Earth and Planetary Science Letters*, 297:154–164, 08 2010.

[30] Jason P. Morgan, Lars H. Rüpke, and William M. White. The current energetics of earth's interior: A gravitational energy perspective. *Frontiers in Earth Science*, 4, 05 2016.

[31] H. Goni, F. Khanom, and T. S. Khaleque. Convection in the earth-like mantle with the influence of strong viscosity variation. *Journal of Applied Mathematics and Computation*, 7(4):443–454, 01 2023.

[32] Sumaiya B Islam, Suraiya A Shefa, and Tania S Khaleque. Mathematical modelling of mantle convection at a high rayleigh number with variable viscosity and viscous dissipation. *Journal of the Egyptian Mathematical Society*, 30, 02 2022.

[33] Simon R W Lance, Laura K Currie, and Matthew K Browning. Viscous dissipation and dynamics in simulations of rotating, stratified plane-layer convection. *Monthly Notices of the Royal Astronomical Society*, 528(4):6720–6734, 01 2024.

[34] Y. Requilé, S.C. Hirata, and M.N. Ouarzazi. Viscous dissipation effects on the linear stability of rayleigh-bénard-poiseuille/couette convection. *International Journal of Heat and Mass Transfer*, 146:118834, 01 2020.

[35] Brian Straughan. Nonlinear stability for thermal convection in a brinkman porous material with viscous dissipation. *Transport in Porous Media*, 134:303–314, 07 2020.

[36] Ben S Knight, J Huw Davies, and Fabio A Capitanio. Timescales of successful and failed subduction: insights from numerical modelling. *Geophysical Journal International*, 225(1):261–276, 09 2020.

[37] Ulrich R. Christensen. Time-dependent convection in elongated rayleigh-benard cells. *Geophysical Research Letters*, 14:220–223, 03 1987.

[38] Benaouda Abbou, Said Mekroussi, Houari Ameur, and Sahraoui Kherris. Effect of aspect ratio and nonuniform temperature on mixed convection in a double lid-driven cavity. *Numerical Heat Transfer Part A-applications*, 83:237–247, 06 2022.

[39] D. P. Mckenzie, J. M. Roberts, and N. O. Weiss. Convection in the earth's mantle: towards a numerical simulation. *Journal of Fluid Mechanics*, 62(03):465, 1974.

[40] V. S. Solomatov. Scaling of temperature- and stress-dependent viscosity convection. *Physics of Fluids*, 7(2):266–274, 1995.

[41] Ulrich R. Christensen and David A. Yuen. Layered convection induced by phase transitions. *Journal of Geophysical Research: Solid Earth*, 90(B12):10291–10300, 1985.

[42] C. Stein and U. Hansen. Arrhenius rheology versus frank-kamenetskii rheology—implications for mantle dynamics. *Geochemistry, Geophysics, Geosystems*, 14(8):2757–2770, 2013.

[43] Jun Korenaga. Scaling of stagnant-lid convection with arrhenius rheology and the effects of mantle melting. *Geophysical Journal International*, 179(1):154–170, 10 2009.

[44] A C Fowler, Peter Howell, and Tania S Khaleque. Convection of a fluid with strongly temperature and pressure dependent viscosity. *Geophysical and Astrophysical Fluid Dynamics*, 110:130–165, 03 2016.

[45] Gary T. Jarvis and W. R. Peltier. Mantle convection as a boundary layer phenomenon. *Geophysical Journal International*, 68(2):389–427, 02 1982.

[46] Donald E. Koglin Jr., Sanaz R. Ghias, Scott D. King, Gary T. Jarvis, and Julian P. Lowman. Mantle convection with reversing mobile plates: A benchmark study. *Geochemistry, Geophysics, Geosystems*, 6(9), 2005.

[47] Gary T. Jarvis and Dan P. Mckenzie. Convection in a compressible fluid with infinite prandtl number. *Journal of Fluid Mechanics*, 96(3):515–583, 1980.

[48] Frédéric Deschamps and Christophe Sotin. Inversion of two-dimensional numerical convection experiments for a fluid with a strongly temperature-dependent viscosity. *Geophysical Journal International*, 143(1):204–218, 10 2000.